Parameter study and experimental analysis of a thermo-mechanical de-icing concept

OPEN ACCESS
IOP Publishing
Smart Materials and Structures
Smart Mater. Struct. **29** (2020) 045021 (14pp)
https://doi.org/10.1088/1361-665X/ab74bc

Parameter study and experimental analysis of a thermo-mechanical de-icing concept

Ozan Tamer[1], **Alexander Kyriazis** and **Michael Sinapius**

Institute for Adaptronics and Function Integration, Technische Universität Braunschweig, Germany

E-mail: o.tamer@tu-braunschweig.de, a.kyriazis@tu-braunschweig.de and m.sinapius@tu-braunschweig.de

Received 24 July 2019, revised 20 December 2019
Accepted for publication 10 February 2020
Published 9 March 2020

Abstract

The removal of ice accumulation on aerodynamic surfaces is a common challenge not only in aviation but also for stationary installations on the ground such as wind turbines. The aim of this paper is to investigate a novel concept for a thermo-mechanical de-icing system based on shape memory alloys. To understand the functional principle in detail, a functional sample is designed, fabricated and experimentally investigated. With a systematic design approach using a morphological box, an optimal configuration is sought and evaluated that harmonizes all relevant functions in the sense of maximum functional conformity. One selected concept forms the basis for the simulation model, which is used to investigate the influence of different parameters on the thermo-mechanical behavior of the functional sample. The results of the parameter study are used to produce a functional sample for investigating the de-icing ability. The experiments on the functional sample serve to validate and improve the simulation model. The comparison of the measurement data with the model prediction shows a good correlation between measurement and prediction with reasonable deviations. The findings on the test methodology, the manufacturing technology and the system behavior allow the further development of the de-icing concept in subsequent steps.

Keywords: de-icing, shape memory alloys, SMA

(Some figures may appear in colour only in the online journal)

1. Introduction

Aerodynamic surfaces tend to ice-up under cold environmental conditions, making them to lose their aerodynamic function. The aim of this publication is to investigate a new concept for solving the icing problem of aerodynamic surfaces which combines a thermal effect with a mechanical effect. Here it is discussed the systematical development of a functional sample with shape memory alloy (SMA) for the investigation of the desired de-icing effect.

Although SMA is a promising material in engineering due to its high energy density, the long cooling time of the material is a challenge for designers, which restricts the application possibilities. The literatures report on some examples of SMA-based de-icing investigations.

The first studies of SMA-based de-icing are presented by Gerardi *et al* [1]. They investigated two de-icing designs for the rotor blade of helicopters. Both reported principles are based on an SMA sheet that creates a strain on the aerodynamic surface that causes the ice layer to delaminate. The results of the tests in the icing tunnel have shown the feasibility of ice debonding by a horizontal shear mechanism of less than 0.2% surface strain. Adams [2] patented a mechanical de-icing system with SMA for airfoils in 1996 (US5558304). In the design, the outer shell contains parts made of SMA that deform with heating. The deformation triggers a deflection of the outer shell, which causes the ice layer to delaminate. Ingram *et al* [3] hold another patent for a

[1] Author to whom any correspondence should be addressed

de-icing system with SMA (US5686003). According to their patent, an SMA sheet is used on the wing to remove the ice layer. The activation of the SMA sheet allows the elastic surface of the wing's leading edge to contract and expand, causing shearing and peeling of the ice layer. Myose *et al* [4] developed SMA composites for de-icing. For this purpose, different semi-circular functional samples manufactured from SMA embedded in fiberglass epoxy composite were tested without aerodynamic loading. Pinto and co-workers [5] developed a multifunctional composite material with SMA whose main tasks were the monitoring of the structural health and the detection of damage. On the other hand, the embedded SMAs increase the temperature at certain parts of the structure to prevent the ice accumulation or melt the ice layer. The work of Sullivan *et al* [6] investigates the feasibility of an SMA based de-icing system in which the leading edge of a NACA 0012 wing made of a thin aluminum sheet is connected to wires made of NiTi SMA. When the wires are activated, contraction takes place that breaks the ice layer. After the test, it turned out that the ice layer was broken with the activation of SMA, but unfortunately the break is not sufficient for the delamination. A recent study [7] reports on a de-icing system for a fixed-wing with SMA sheet and examines numerically the essential properties of the concept.

SMA based de-icing concepts have received much attention over the last two decades either as a mechanical de-icing system or as a thermal de-icing system. This paper proposes a novel approach to the thermo-mechanical de-icing system with SMA for the aerodynamic surfaces by using temperature rise and mechanical contraction of the material together, which makes SMA a natural born hybrid de-icing system.

In most cases, the term 'aerodynamic surface' is initially associated with the wings of aircraft. Even though mainly aircraft wings are strongly affected by the icing problems, further examples of aerodynamic surfaces with icing problems are given here in order to better capture the term 'aerodynamic surface' in its general meaning. Wind turbine blades are a class of aerodynamic surfaces for which the literature explicitly mentions an icing problem when it is used in cold regions.

In the case of aircraft wings, icing causes a considerable deterioration of the lift coefficient. At the same time, the stall angle, i.e. the profile angle at which the airflow breaks off, is reduced. Icing on the elevator can furthermore cause the aircraft to experience a tilting moment, and tilt its nose forward. Moreover icing on the ailerons can additionally affect the aircraft's roll behavior [8]. Icing can therefore affect all flight maneuvers and may lead to a crash of the aircraft if the ice accumulation exceeds a critical level.

Ice layers are formed at temperatures between 0 °C and −20 °C by supercooled water droplets. The physical limit temperature for supercooled water droplets is −40 °C. Below this temperature limit, water droplets occur only in frozen form. If such a supercooled water droplet hits a surface, it freezes immediately because it is thermodynamically unstable, and the transition from liquid to solid occurs with a small external stimulation. Over time, a thicker ice layer forms, which may lead to the problems described above [8].

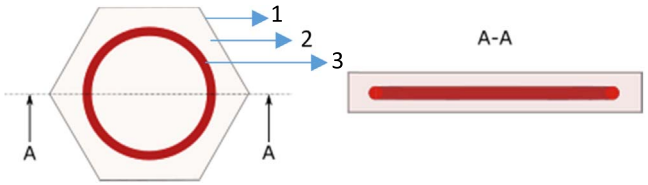

Figure 1. Illustration of the de-icing concept (1. De-icing segment, 2. Elastomer, 3. SMA-ring).

Approaches to avoid ice accumulation on aerodynamic surfaces can be divided into ice prevention and de-icing. Ice prevention aims to prevent the formation of ice layers from the outset [9]. De-icing serves to remove accumulated ice layers by mechanical or thermal means. The thermo-mechanical de-icing concept presented in this article is suitable for the cyclic removal of ice.

The new concept uses an annular SMA embedded in an elastomer as a thermo-mechanical de-icing system, see figure 1. In order to investigate the effects of stiffness ratios and other material parameters, a functional sample based on a hexagonal shape which at the same time serves as a basic element of a planar arrangement, is investigated.

The hexagonal shape minimizes the dead areas that remain covered with ice. For this purpose, a large number of such de-icing segments are combined on the air flow surface.

Table 1 sketches the functional principle of the de-icing segment in the activated state of the SMA. The activation of the SMA ring causes contraction, which results in a bump in the elastomer on the surface. This is the mechanical effect of the de-icing process. At the same time, the activation of the SMA ring influences an increase in surface temperature. This is the thermal part of the de-icing process. This combined thermo-mechanical load removes ice layers from the aerodynamic surface. The mechanical force on the ice layer results from the shape memory effect. The actuating heat of the SMA is also used to reduce the holding power of the ice.

The objective of our study is to investigate the thermo-mechanical de-icing principle and gain insights for the later implementation of the approach. For this purpose, a simulation model is created and a functional sample is realized. The simulation model serves to reveal the correlations between geometry parameters, force development and heat transfer during actuation.

The procedure chosen for the development of the functional models is divided into five main phases: planning, conception, design, elaboration and investigation. The first four phases originate from the product development process according to Pahl and Beitz [10]. The fifth phase takes into account manufacturing and experimental investigation.

2. Theoretical background

2.1. Shape memory alloys

SMAs are classified as 'Smart Materials' because they respond to temperature changes and mechanical stress. A unique property of SMA is that by increasing the material temperature, the material can change its shape into a memorized form. The most common type of alloy to exhibit this effect is certainly Nitinol, which is composed of approximately half nickel and half titanium.

The shape memory effect is the property of the alloy that enables shape recovery. Here the alloy is loaded in the martensitic phase and then unloaded while the temperature is still below than A_s (austenite start temperature). By raising the temperature to A_f (austenite finish temperature), the alloy gains its original shape by the transformation into the austenitic phase. The phenomenon is also called a one-way effect because in this effect the shape is recovered by heating after the material has been detwinned by an applied mechanical load [11].

Another characteristic is that SMAs can create repetitive deformations by allowing the material temperature to oscillate between A_f and M_f (martensite finish temperature) without mechanical load. This property is called a two-way effect and emerges when the SMA material experiences a repetitive thermo-mechanical cycle along a particular loading route, which is also known as training [11].

The so-called training process causes the forward transformation ($A \rightarrow M$) to take place through the internal stress fields (intrinsic). If the reshaping takes place through external force, this is called an extrinsic two-way effect. In this case, the reversible change in shape is achieved in principle by the fact that the one-way effect is induced repeatedly by an external, deforming force [12].

The concept presented in this paper combines SMA and elastomer. The spring force of the elastomer is acting as an additional external force so that the SMA can be re-strained again.

2.2. De-icing mechanics

The explanation of the thermo-mechanical de-icing principle first requires the clarification of the stress state in the contact zone between ice and structural surface.

Nine different mechanical stresses act on a volume element from the contact zone of the ice layer and the underlying structure in a coordinate system whose z-axis is perpendicular to the contact surface, see figure 2, six shear stresses τ_{xy}, τ_{xz}, τ_{yx}, τ_{yz}, τ_{zx} and τ_{zy} and the three normal stresses σ_x, σ_y and σ_z.

Taking into account the assigned shear stresses, i.e. $\tau_{ij} = \tau_{ji}$, there are only three independent shear stresses and three normal stresses. The shear stresses in the contact plane τ_{zy} andτ_{zx} act as interlaminar shear stresses. By considering the ice layer and the underlying structure as a composite material, Palacios [13] elaborated that the delamination of the ice layer is caused by these interlaminar shear stresses. Therefore, the Euclidean sum τ_v of τ_{zy} and τ_{zx} is used as the

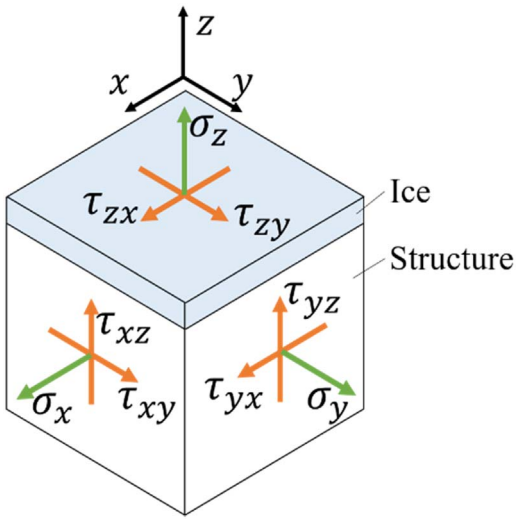

Figure 2. Stresses on a cut free volume element.

criterion for the separation, as [14] also use with neglected normal stress σ_z:

$$\tau_v = \sqrt{\tau_{zy}^2 + \tau_{zx}^2}.$$

The different de-icing concepts are evaluated on the basis of the comparative shear stress given above. If the shear stress locally exceeds the temperature-dependent adhesive strength of the ice layer, the ice detaches locally from the basic structure. According to [15], the adhesion strength of ice decreases with increasing temperature from −13 °C to 0 °C.

Due to the temperature dependence of the ice adhesion strength, the combination of a mechanical effect with a thermal effect appears to be reasonable. However, melting of the ice surface should be avoided, since the ice layer loses its surface adhesion due to the liquid film forming, and thus no more shear stresses can be transferred to the ice layer.

2.3. Polymers and polymer composites

The properties of the elastomers are outlined in this section because the proposed thermo-mechanical de-icing concept is based on embedding an SMA wire into an elastomer.

Many elastomers are capable of being elastically elongated to multiple of their initial length with the application of force [16]. Elastomers are permanently used above its glass transition temperature and exhibit entropy-elastic behavior. This is based on the fact that the entropy in the stretched state is lower than in the undeformed state. This can be explained by the number of implementation phases. According to the second law of thermodynamics, the elastomer deforms back to its original shape, as entropy increases [17]. However, the reached recovery forces are rather low, as a result of low moduli of elasticity.

Polymers generally have a low thermal conductivity compared to metals. By reinforcing those, both the mechanical and thermal conductivity properties can be improved. The mechanical properties are usually achieved by fiber reinforcements. Embedded fibers increase the stiffness of the plastic in the fiber direction. Glass fibers, carbon fibers and fibers

Table 1. Representation of the effect with SMA activation.

Effect	Initial State	SMA activated
Mechanical		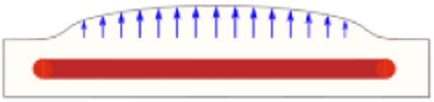
Thermal		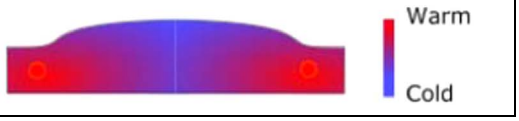

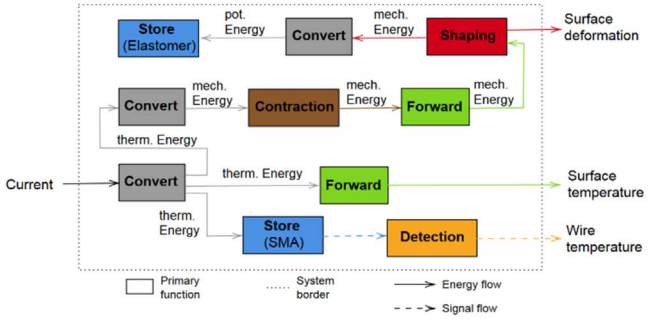

Figure 3. Functional structure during actuation phase.

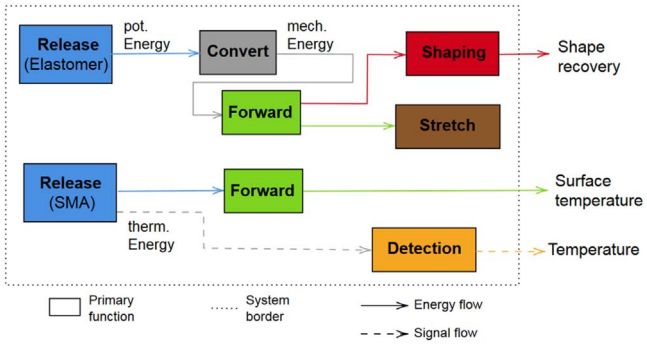

Figure 4. Functional structure during reset phase.

made of high-strength polymers such as aramid have established for use in fiber-reinforced polymers [18].

3. Principal concept definition

3.1. Functional structure

The key idea of the concept is to use an elastomer membrane with an embedded SMA wire. In order not to exclude any solutions in advance, an abstraction of the main function is carried out in a first step. This shows a mechanical deformation of the surface and a simultaneous increase of the surface temperature form the main tasks of the de-icing system. Electrical energy is available as input energy.

If the functions are formulated in a more detailed functional structure, it is worth distinguishing between the actuation phase and the reset phase, see diagrams presented in figures 3 and 4. In the figures, the '*convert*' blocks represent the conversion of electrical energy into thermal energy or thermal energy into mechanical energy. '*Store*' and '*release*' refer to the steps, where energy saved in or recovered from elastomer or SMA as a potential or thermal energy source. '*Forward*' represents the transport of energy through the functional sample.

In the actuation phase (figure 3), electrical energy (current) is converted into thermal energy by the Joule effect. The thermal energy, in turn, is divided into two parts: a part that is utilized to heat the surface and a part that is converted into mechanical energy via the shape memory effect (contraction). The mechanical energy is partly stored in the elastomer for the reset phase and in part used to deform the ice surface. In the reset phase (figure 4), the stored mechanical energy is used to return the shape memory actuator to its pseudo-plastically stretched shape and to recover the membrane's surface shape. For these abstract functions, solutions can be found and represented in a morphological box [10]. The morphological box is suitable for a systematic solution search. According to this scheme usually only the main functions and the belonging solutions are entered in the columns [10].

3.2. Methodical concept development

The basis of the further concept development is that the potential energy is stored in the elastomer membrane in the sense of a spring. Table 2 shows a morphological box that combines possible solutions for the remaining subfunctions of the concept to be found. These are:

a. supply form of mechanical energy from the shape memory effect,
b. mode of membrane deformation,
c. type of heat conduction to the surface,
d. conduction of the mechanical energy to the surface.

The morphological box leads to different concepts, which are evaluated on the basis of the following criteria for a selection:

Table 2. Morphological box for the search for concepts.

Functions \ Solutions		1	2	3	4	5
A	Mechanical energy form	Tensile / compressive, uniaxial	Tensile / compressive, biaxial	Bending	Circumferental contraction	Shear
B	Mode of membrane deformation	Normal force	Excentrical tangential force	Induced bending moment		
C	Heat conduction	3D heat conduction through elastomer	2D heat conduction through metall sheet	1D heat conduction through metal rod	1D heat conduction through carbon fibres	0D heat conduction through metal particles
D	Conduction path for mechanical energy to membrane	Application on surface	Integration	Kinematic	Conduct through fluid	

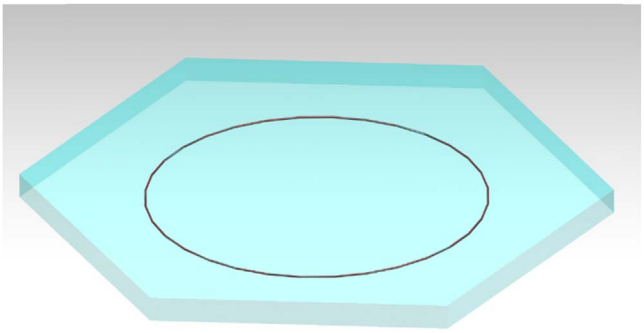

Figure 5. Concept of the functional sample in CATIA V5.

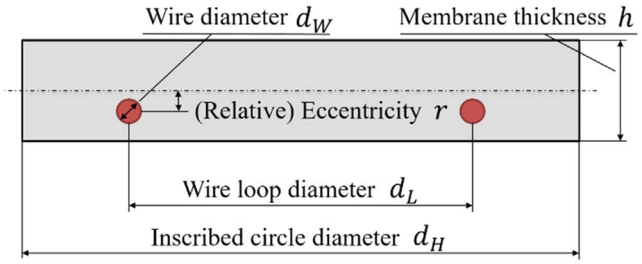

Figure 6. Geometric parameters of the functional sample.

(i) heat conduction to the surface,
(ii) estimated manufacturing effort,
(iii) achievable accuracy,
(iv) estimated deformation,
(v) system complexity,
(vi) required installation space,
(vii) number of optimization parameters offered by the concept.

The selected concept is highlighted in figure 5 and provides a closed-loop of shape memory wire to be embedded into the elastomer membrane. Due to the eccentric (displaced in the perpendicular direction to the membrane surface) arrangement of the wire loop, a bending moment occurs in the elastomer membrane, which leads to a curvature of the membrane. The heat conduction is effected by the elastomer material of the membrane, an improvement of the heat conduction by introducing metal particles is provided for further investigations.

In further detailing the concept, it was decided to design the functional sample in a hexagonal basic shape and electrically contact to the wire loop on two opposite sides. Figure 5 shows a CAD model of the concept. A detailed parameter study yields the final dimensions as explained below.

3.3. Parametric design specification

The concept shown in figure 5 can be geometrically described by five parameters sketched in figure 6. The diameter of the SMA wire and the loop are describing the geometry of the wire loop. The diameter of the hexagon, which describes the contour, and the thickness of the membrane represent the elastomer membrane geometry. The relative position of the wire loop to the elastomer membrane is described by a parameter called eccentricity.

Since Nitinol is used as a SMA, it is material properties are already fixed. On the other hand, the properties of the elastomer to be used are still free design parameters. Its material characteristics are examined as a part of the parameter study. This adds the following three material parameters to the geometric parameters, as shown in figure 6:

- modulus of elasticity,
- thermal conductivity,
- heat capacity.

The thermal conductivity and heat capacity are used to model the heat transfer from the wire to the surface of the

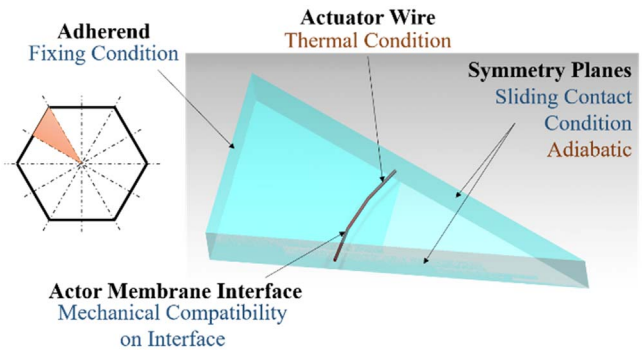

Figure 7. One-twelfth model and conditions for representing symmetry and external mount.

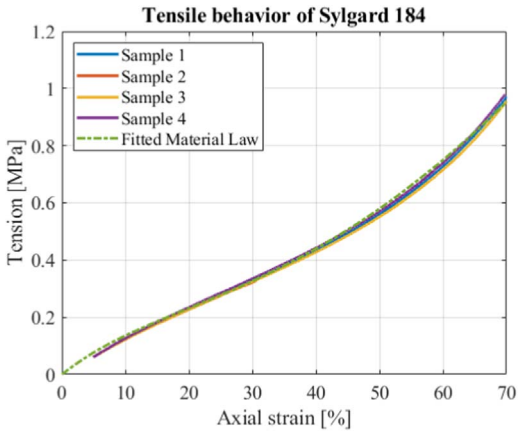

Figure 8. Mooney–Rivlin material law fit.

functional sample. The modulus of elasticity is to be interpreted as the slope of the nonlinear stress–strain curve for low strains, since a simple hyperelastic material law (Neo Hooke) is used to model the behavior of the elastomer:

$$E = \frac{\partial \sigma}{\partial \varepsilon}\bigg|_{\varepsilon=0}.$$

The Neo Hooke material model is based on a formulation of the elastic energy as a function of the deformation of the material which is assumed to be incompressible [19]. As a measure of the deformation, the stretch λ is used, which is related to the strain ε as follows:

$$\lambda = 1 + \varepsilon = \frac{l}{l_0},$$

where l_0 stands for the unstretched length and l for the length after deformation. In the Neo-Hooke material model, the elastic energy results from the stretches λ_1, λ_2 and λ_3 in three directions:

$$W_{mech} = C \cdot (\lambda_1^2 + \lambda_2^2 + \lambda_3^2).$$

The constant C depends on the linear modulus of elasticity E, which can be used to describe the material for minor deformations.

4. Numerical simulation and parameter study

4.1. Numerical simulation model

The influences of the geometry and the elastomer on the behavior of the concept are examined by means of a parameter study. For this purpose, a model of the functional sample is created.

Considering the symmetries of the functional sample, the model is reduced to a one-twelfth model, see figure 7. The symmetries are implemented as additional boundary conditions at the intersections. So the symmetry leads to the fact that the section surface must be regarded as adiabatic, since a heat flow over the section surface would mean a violation of the symmetry. Furthermore, all nodes lying on a plane of symmetry cannot deviate from it. Deviating from the plane of symmetry would again be a violation of the symmetry condition.

The outside of the functional sample is glued into an external fixture. In the model, the related boundary condition is defined as perfectly isolated and rigid. Subsequent tests have shown that these assumptions are well fulfilled by the functional sample.

Both the shape memory wire and the elastomer membrane are meshed in the finite element (FE) model with tetrahedral volume elements. The actuator wire is embedded into the elastomer membrane with three prismatic layers in order to accurately simulate the force transfer. The connection of the wire to the elastomer is rigid in the model, i.e. no relative movement is assumed between wire and elastomer. The wire is modeled as a heat source by assigning it to a fixed temperature of 100 K above the ambient temperature. This allows a quick comparison of the different thermal conductivities of different geometries. However, this modeling is too imprecise for a detailed simulation of the thermal dynamic behavior.

Since large deformations occur inside the functional sample, it behaves geometrically nonlinear. The hyperelastic behavior of the material represents a further nonlinearity. The application of the Newton–Raphson algorithm enables these nonlinearities to be taken into account in an iterative solution process with step size limitation.

4.2. Material models and parameters

The Neo-Hooke material model is best suited to be used in the parameter study, as it can be varied effortlessly via the stiffness parameter C which is related to the tangent slope of the stress-strain curve for small strains ε (classical linear modulus of elasticity) as follows:

$$C = \frac{E}{6}.$$

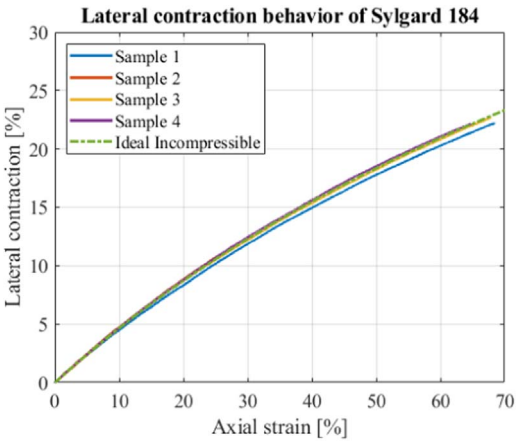

Figure 9. Sylgard 184 can be assumed to be incompressible.

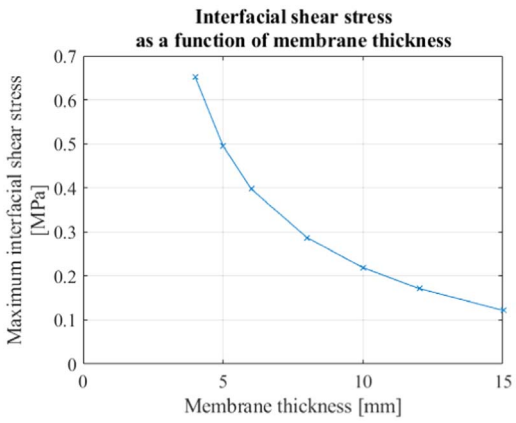

Figure 10. An increase in membrane thickness reduces the shear stresses developed in the ice-elastomer interface.

Table 3. Material parameters for Mooney–Rivlin curve fit.

Parameter	C_{01}	C_{10}	C_{11}
Value	0.66 MPa	−0.36 MPa	0.24 MPa

The parameter study leads to the selection of the elastomer Sylgard 184 for further experimental investigations. The material behavior of the elastomer can be described for design with the more precise Mooney–Rivlin material law:

$$W_{mech} = C_{01} \cdot (I_1 - 3) + C_{10} \cdot (I_2 - 3) + C_{11} \cdot (I_1 - 3) \cdot (I_2 - 3),$$

where $I_1 = \lambda_1^2 + \lambda_2^2 + \lambda_3^2$ and $I_2 = \lambda_1^2 \cdot \lambda_2^2 + \lambda_2^2 \cdot \lambda_3^2 + \lambda_1^2 \cdot \lambda_3^2$ are the invariants of the nonlinear stretch tensor. A curve fit to the results of a four specimen tensile test (see figure 8) provides the remaining parameters C_{01}, C_{10} and C_{11}. Table 3 lists the resulting parameters. The Mooney–Rivlin model also requires the incompressibility of the elastomer. Figure 9 shows that this assumption is well fulfilled in reality. The dotted green curve represents an ideally incompressible material behavior, the solid lines represent the tensile specimens from Sylgard 184.

The FE method is suitable to model the shape memory effect with the associated material parameters at any temperature between M_f and A_f. Here, however, it is only necessary to describe the initial and activated shapes of the alloy, since the interstate of the transformation is of secondary importance for the design. The elongation due to the shape memory effect is represented in the model by thermal expansion due to the temperature difference of 100 K. To ensure that the effect always occurs in the circumferential direction, a polar coordinate system is defined for the wire loop. The thermal expansion of the elastomer is negligibly small compared to the expansion effect of the SMA and is therefore not considered in the simulation.

4.3. Evaluation of extreme cases

The challenge in modeling is that ice layers on aerodynamic surfaces can be of different thicknesses and consist of different ice types. Consequently, it is not possible to define a specific thermal and mechanical resistance against which the functional sample must work during a de-icing cycle. Therefore, the alternative approach chosen in this study is to investigate the range where the typical deformations and stresses are located. The extreme cases for both mechanical and thermal behavior are suitable to describe the field of application. The mechanical and thermal behaviors are studied individually instead of a coupled system.

The first mechanical extreme case is a highly stiff ice layer. The model takes this extreme case into account by completely blocking the movement of the upper effective surface of the functional sample. On the other hand, the extreme case of a thin, flexible ice layer is considered. In the model, this is taken into account by the fact that the upper effective surface can move freely. It is obvious that in the first extreme case large stresses occur in the upper effective surface and in the second extreme case large deformations are to be expected. In order to be able to compare the simulation results of different parameter sets with each other, it is determined in the case of a highly stiff ice layer that the maximum shear stresses in contact between the ice layer and functional sample are compared. In the case of a particularly flexible ice layer, the maximum strains in the surface are considered.

Two similar extreme cases are considered for the thermal behavior. In the first extreme case, the active surface behaves adiabatically. This corresponds to the case where the functional sample is almost thermally insulated by a quite thick layer of ice. In the second extreme case, the temperature of the active surface corresponds to the ambient temperature, which corresponds to heat dissipation by convection in the airstream. In this case, different geometries are evaluated using the heat flux density of the surface.

In thermal modeling, the described simplification of the ice layer by extreme cases is urgently necessary because here the heat flux conditions, as well as the thickness and composition of the ice layer, are unknown though have a great impact. On the whole, the consideration of extreme cases makes it possible to completely eliminate the ice layer dependent parameter influences from the parameter study.

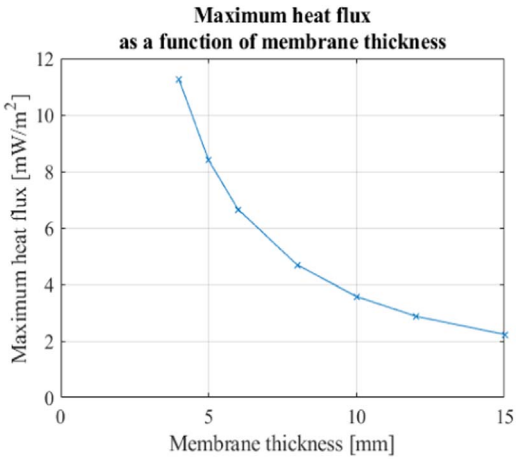

Figure 11. An increase in membrane thickness causes a decrease in the maximum heat flux density.

4.4. Parameter study

The parameter study revealed a number of several correlations between input parameters and the thermo-mechanical behavior of the functional sample. In particular, the membrane thickness has a dominant influence on the thermo-mechanical behavior of the functional sample. Also, the mechanical tensile stress in the SMA wire, the heat conduction from the wire to the surface and the shear stress achieved on the surface are influenced by the membrane thickness. In all investigations, the SMA wire's relative position within the elastomer membrane is the same. The SMA wire is always three-quarters of the membrane thickness away from the surface.

Both the heat conduction and the achieved shear stress in the surface show a decreasing curve depending on the membrane thickness, see figures 10 and 11. In the case of heat conduction, the decreasing curve is due to the thermal resistance, which increases with the heat conduction distance through the elastomer and thus reduces the transported heat flow.

The decreasing shear stress (see figure 10) is due to the fact that the shear stress has to be transferred from the force initiation of the SMA wire via the elastomer to the surface. The longer the transmission distance, the higher the internal deformations in the elastomer and the lower the effective shear stress at the surface. The dimensions of the functional sample in the surface plane have a minor influence both on the thermal conductivity behavior and on the shear stresses.

The membrane thickness has the opposite effect on the tension in the shape memory wire. The thicker the elastomer membrane, the higher the stress in the shape memory wire because of the increasing stiffness of the elastomer membrane (both multi-axial bending stiffness and compressive stiffness). At this point, however, the limits of simplified modeling of the shape memory effect can also be seen. While the model based on thermal expansion predicts tensile stresses of up to 4 GPa, the real shape memory wire would build up irreversible plastic deformations starting from tensile stresses of the order of 700 MPa. However, such high stresses are to be avoided during operation.

Table 4. Geometric parameters of the functional sample.

Membrane thickness (h)	8 mm
Relative eccentricity (r)	−50%
Diameter of inscribed circle (d_H)	120 mm
Wire loop diameter (d_L)	80 mm

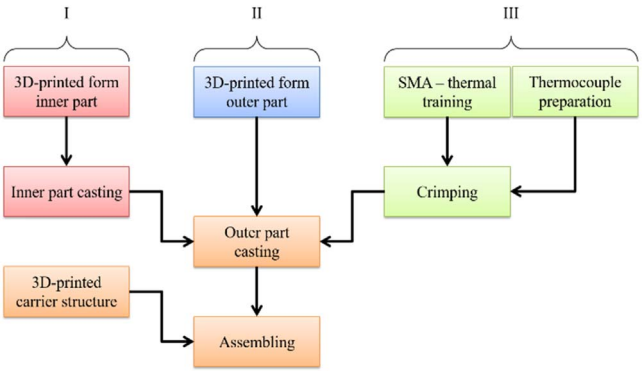

Figure 12. Manufacturing sequence for a functional sample.

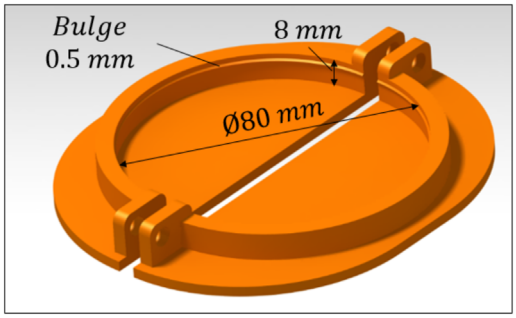

Figure 13. Mould for the inner part of the elastomer membrane.

The central aspect of the design is to achieve structural conformity between SMA wire and elastomer. If the SMA wire is too thin, its stiffness is too low compared to the stiffness of the elastomer membrane so that the wire cannot deform it. If the wire is too thick, the stiffness of the elastomer membrane will not be sufficient to reshape the wire after actuation. The most important criterion here is the tensile stress in the wire. In design, a wire with a diameter of 375 μm inducing a tensile stress of approx. 400 MPa during operation optimally met the requirements for structural conformity. All remaining parameters resulting from the design process are listed in table 4.

5. Manufacturing of functional sample

It is to be expected that the manufacturing process will have an influence on the de-icing properties. Therefore, the manufacturing process is investigated in this section.

5.1. Elastomer membrane formation

The manufacturing plan is used to obtain an overview of the materials required and the logical sequence of the production

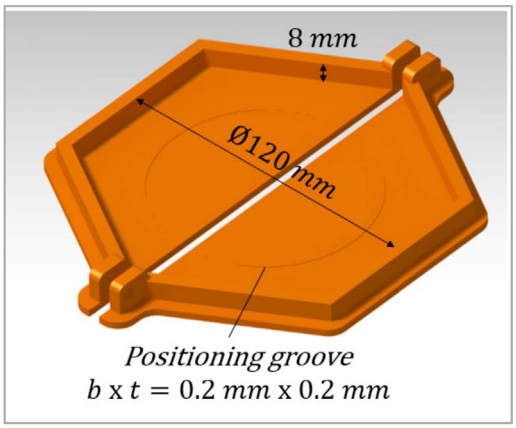

Figure 14. Mould for the outer part of the elastomer membrane.

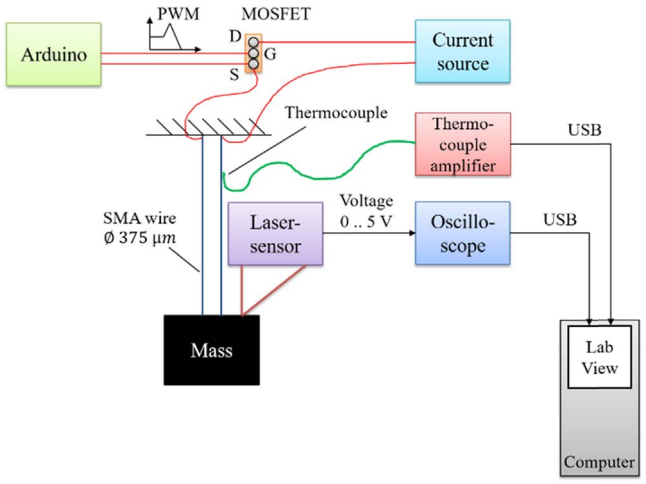

Figure 15. Block diagram for data acquisition during thermal training.

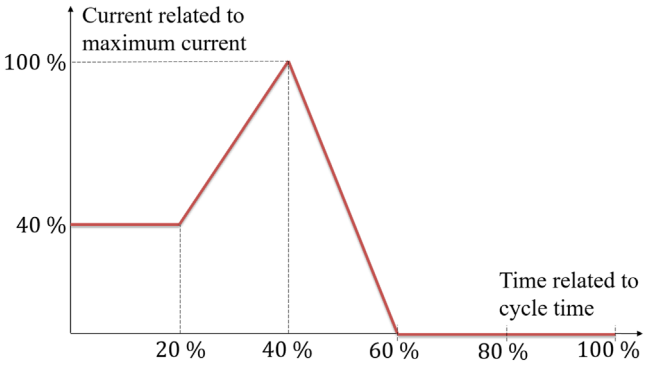

Figure 16. Course of the current during thermal training.

steps. Manufacturing initially runs in three parallel lines, see figure 12.

In the first manufacturing line, the inner part of the functional sample is prepared, see figure 13. First, a casting mould made of polylactide (PLA) is produced in the 3D printer.

Both moulds consist of two parts in order to enable the demoulding of the finished cast part. The inner part of the elastomer membrane has a groove for precise positioning of the wire loop. The height of both moulds is designed to fill them to the edge during casting so that the resulting elastomer casting has the desired membrane thickness of 8 mm.

In the second manufacturing line, a mould for casting the outer part of the functional sample is printed. The shape of the outer part is also 8 mm deep. A circular groove (0.2 mm wide and 0.2 mm deep) is made in the outer mould to position the already casted inner part of the elastomer membrane in order to visually support the centering of the mould. The outer shape of the functional sample is hexagonal with a diameter of 120 mm, see figure 14.

The third manufacturing line concerns the preparation of the actuators. The first step is the thermal training of the SMA wire. In the second step, an active loop is created from the SMA wire and the electrical contacts by crimping. In addition to the SMA wire and the electrical contacts, a thermocouple for integrated temperature monitoring is embedded into this loop too.

During the casting of the outer part, the three manufacturing lines are combined. For this step, the casted inner part, the wire loop and the casting mould for the outer part are required. The final step in production is the final mechanical positioning of the functional sample. For this purpose, a mechanical carrier structure must first be produced using 3D printing. The finished functional sample is then glued into its outer carrier structure.

5.2. Thermal training of SMA-actuator

Thermal training is used to avoid plastic elongation in the SMA wire after embedding it into the elastomer membrane and stabilize the actuation effect. If the plastic strain would build up after embedding, the actuation effect would be degraded. In addition, thermal training causes the extrinsic two-way effect to be supported by an intrinsic two-way effect. Besides, the SMA wire has the desired effect elongation after thermal training.

The thermal training is carried out according to the wire manufacturer's recommendation under mechanical stress of 190 MPa [20]. The heating of the wire is achieved by resistance heating.

The wire reaches a temperature of about 90 °C and a voltage drop of 0.9 V with a current of 1.4 A. The relationship between the amperage and steady-state temperature is disturbed by airflow around the wire and room temperature.

The training setup for executing the thermal training is shown in figure 15. In order to thermally cycle the SMA wire, it is electrically powered with a special current profile. This leads to slower temperature progressions, so that the thermal inertia of the thermocouples used for measurement is less affected. The amperage is varied by a microcontroller that drives a field-effect transistor (MOSFET) via pulse width modulation.

To collect the measurements, the thermal training setup is extended by a laser triangulation sensor, whose displacement signal permits the calculation of the wire strain, and by a thermocouple (type *K*, defined up to $T > 1000\,^{\circ}\mathrm{C}$), which measures the wire temperature.

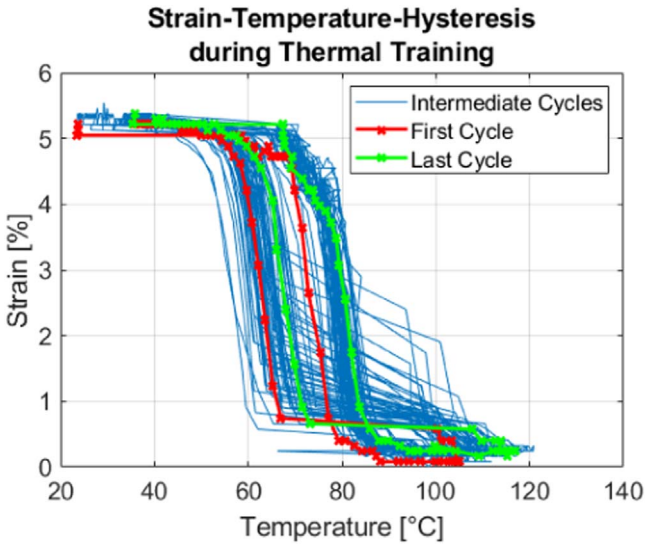

Figure 17. Thermal training of 375 μm SMA wire.

Table 5. Transformation temperatures of the wire.

A_S	A_F	M_S	M_F
70 °C	85 °C	75 °C	60 °C

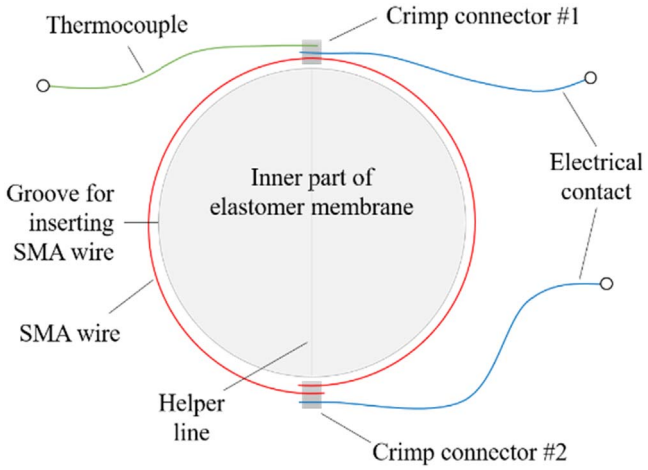

Figure 18. Alignment of the wire to the inner casting.

The time history of the electrical current is shown in figure 16 and the strain-temperature relations are graphically presented in figure 17. The first and last actuation cycles are highlighted in color.

The effect yields an elongation of about 5%. The transformation temperatures determined from the hysteresis curve of the last cycle are given in table 5.

The scattering in the measurements is caused by rotation and lateral movement of the mass and by varying conditions of convective cooling. Investigations with a thermal imaging camera show that the temperature of the wire is not constant over its entire length. A high cycle time causes the wire to slowly heat up and cool down, thus improving the precision of the temperature measurement. On the other hand, it leads to long-lasting measurements. The cycle time of 90 s is a compromise between these two requirements. Training a wire over 50 cycles takes 75 min with this cycle time.

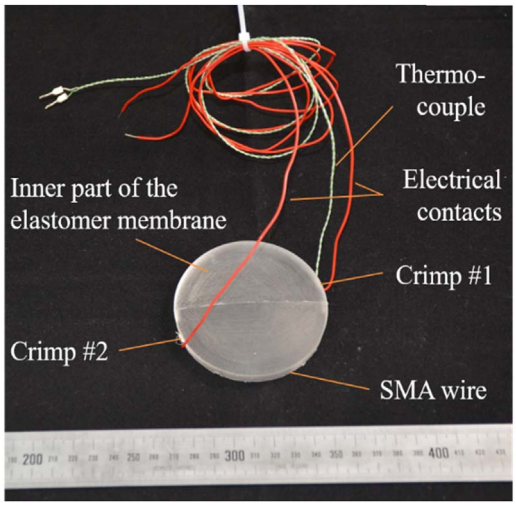

Figure 19. Inner part of the elastomer membrane after placing the wire and thermocouple.

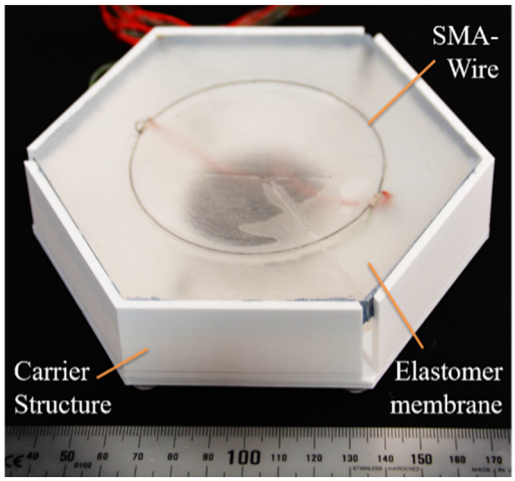

Figure 20. Assembled functional sample with carrier structure.

5.3. Assembly

In the assembly process, the SMA wire is brought into the ring form, electrically contacted and fitted with the thermocouple. The configuration of the assembly is shown in figure 18.

In order to achieve a pretension in the wire, the wire loop is slightly shortened after aligning the crimp just before it is fixed.

The finished loop is then inserted into the groove provided for this purpose in the inner part of the elastomer membrane which has a slight curvature, due to the pre-tension. Figure 19 depicts the resulting assembly of the inner part of the elastomer membrane and the SMA wire loop.

The main purpose of mounting the elastomer membrane with integrated SMA wire in the outer mounting is to realize the fixation conditions of the side surfaces simulated in the FE model. The outer holder is connected to the elastomer

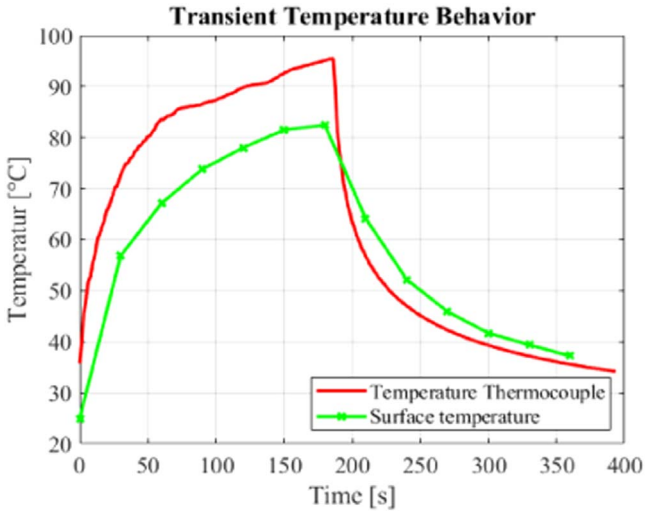

Figure 21. Thermal transient behavior of the functional sample.

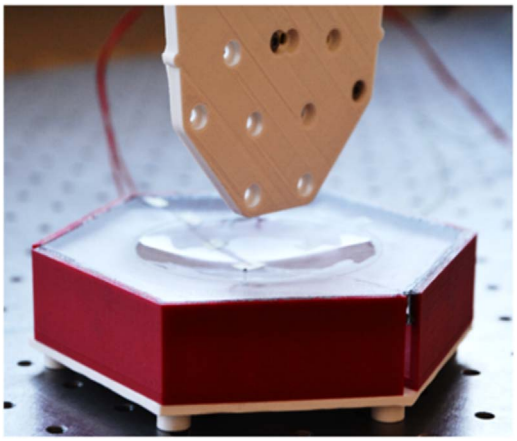

Figure 22. Temperature-displacement hysteresis measurement.

membrane using Dow Corning 7091 adhesive, which is suitable for connection with thermoplastics.

In a final step, the membrane is mounted into the housing free from tension. Figure 20 shows a finished functional sample.

6. Experiments on functional sample

6.1. Thermal testing

During the investigation of the thermal-stationary behavior, the functional sample is actuated with different amperages. After setting an amperage value, the system is actuated until the thermocouple, which is attached to the embedded SMA wire, indicates a stationary temperature. In addition, the required voltage for the functional sample is recorded, and the supplied power is calculated.

At a steady amperage of 2.6 A ($U = 2.1$ V), the mechanical deformation of the functional sample can be observed as a result of the wire actuation. Beyond 2.6 A, this deformation does not increase further. Thus, the functional

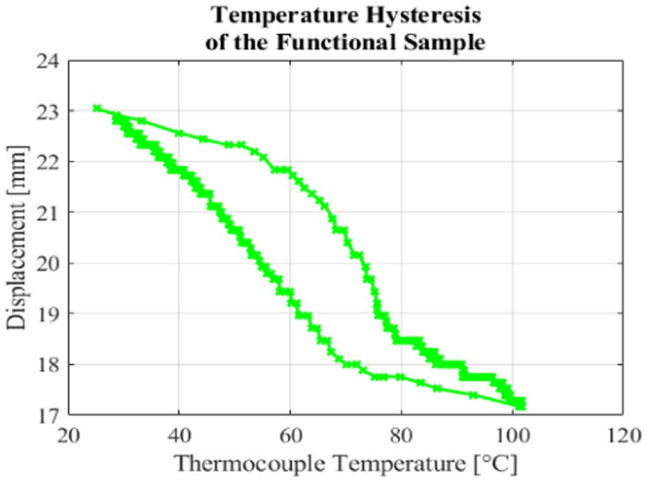

Figure 23. Temperature-deformation hysteresis of the functional sample.

sample is operated at room temperature with a current of 2.6 A.

The thermal transient response shown in figure 21 refers to the dynamic behavior of the temperature distribution within the functional sample and on its surface during a six-minute actuation cycle. The surface temperature is measured with a thermal imaging camera and the wire temperature with the integrated thermocouple. An actuation cycle consists of a three-minute actuation phase and a three-minute cooling phase.

6.2. Mechanical testing

In addition to the thermal transient analysis, the relationship between the temperature of the thermocouple and the deformation in the middle of the functional sample is also determined with the test setup shown in figure 22.

The mechanical-static response includes the magnitude of the actuation effect of the membrane and the degradation of this actuation effect through the number of cycles. Possible reasons for the degradation are plastic creep of the elastomer under combined thermal-mechanical stress, the accumulation of plastic deformation in the SMA wire due to the counter-force of the elastomer membrane, and the build-up of a pre-load in the SMA wire during re-deformation after the first actuation. Such internal stress is necessary to deform the wire back to its initial position using the extrinsic two-way shape memory effect.

The relationship between displacement and temperature is shown in figure 23 exhibiting pronounced hysteresis behavior. It's not only the thermal hysteresis of the SMA wire contributing to the hysteresis curve, but also the viscoelastic behavior of the elastomer.

To investigate the mechanical effect, the surface of the functional sample is measured at six different points, as shown in figure 24. The measured surface data is represented as point plots.

Figure 25 shows deformation from simulation and experiment in a point plot. The simulated deformations are

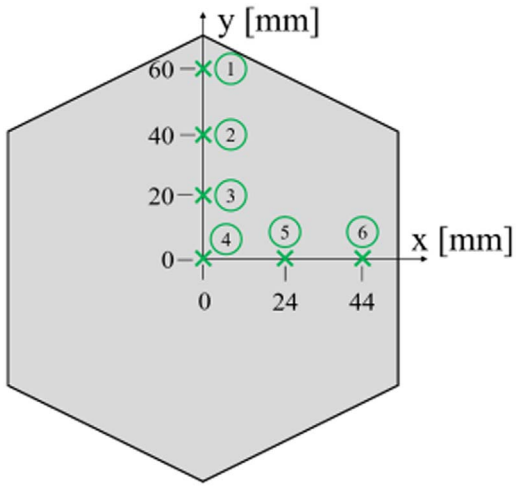

Figure 24. Measuring points for profile measurement of the deformation of the functional sample.

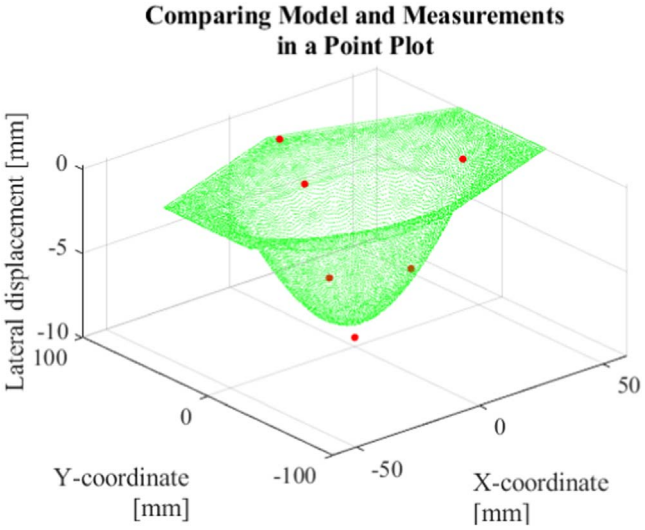

Figure 25. Point plot for the functional sample.

shown in green and the stroke measured during the first actuation is shown in red.

The qualitative comparison in figure 25 shows a good agreement between the measured data and the prediction of the simulation. The measured deformation in the center is slightly larger than the prediction from the simulation. The measurement gives a stroke of 9.46 mm, while the simulation predicts 8.56 mm, which corresponds to a measurement deviation of 10.5% compared to the simulation.

6.3. Iced state examination

A freezer with a temperature of approximately −15 °C is used to examine the functional sample at low temperatures and in the iced state of the surface. The transient temperature behavior at low temperatures is first recorded without an ice layer. The same actuation cycle is used for the investigations at room temperature. The functional sample is first actuated for three minutes at 2.6 A and then cooled without current for

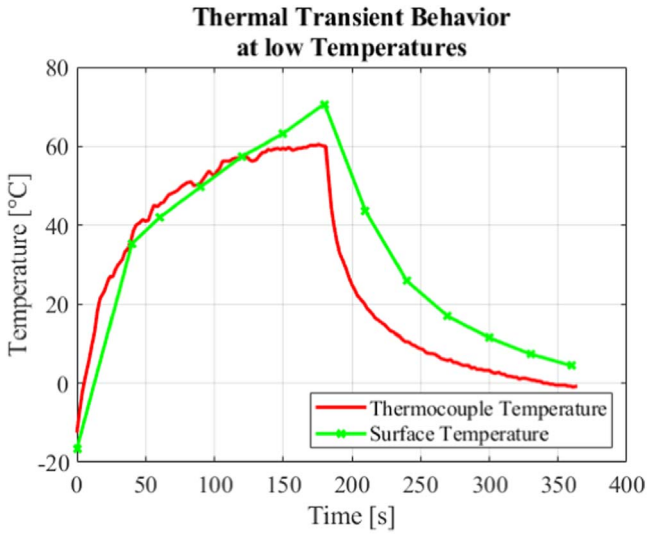

Figure 26. Transient temperature behavior of the functional sample at low temperature.

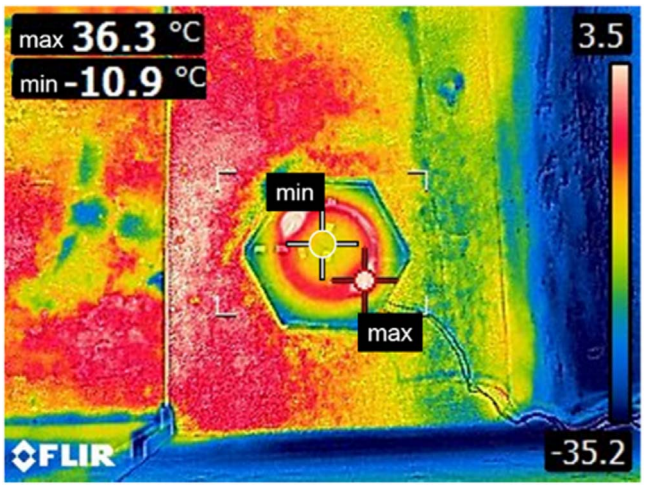

Figure 27. Maximum and minimum temperature on the surface during the actuation.

three minutes. Figure 26 shows the temperature curves of the thermocouple and the surface of the functional sample.

Figure 26 shows that the temperature of the thermocouple reaches just 60 °C after three minutes of actuation. It can also be observed that the maximum surface temperature of 70 °C is higher than the temperature of the crimp connection. This can be attributed to the fact that the temperature of the second crimp connection (without thermocouple) exceeds the temperature of the crimp connection in which the thermocouple measures. It is very likely that the transition resistances in the second crimp connection are greater than in the first crimp connection, which is why the heat dissipated in the second crimp connection is greater.

For testing the de-icing performance, the functional sample is therefore driven with a maximum current of 3.2 A to achieve actuation despite the low ambient temperatures. The thermocouple measures a temperature of 103.75 °C after a switch-on time of 15 min, while the maximum surface temperature is 106 °C.

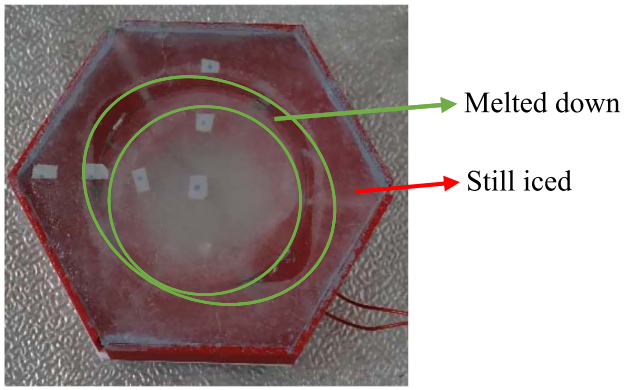

Figure 28. Ring-shaped melting of the ice layer in a de-icing test.

A non-homogeneous ice layer with a thickness of 2–3 mm is produced on the surface by spraying water. The temperature distribution of the surface is examined with a thermal imaging camera (FLIR E8 WiFi). To determine the emissivity e, the surface temperature is measured with a thermocouple and compared with the thermal imaging camera for $e = 0.95$. Figure 27 shows the highest and the lowest surface temperature of the functional sample at the end of the actuation phase.

Actuation of the functional sample cannot be observed in the experiment despite the increased current intensity. It can be assumed that the SMA wire does not exceed the activation temperature. As a result, only the melting of the ice layer in a ring-shaped area above the SMA wire can be observed, see figure 28.

It must therefore be stated that thermo-mechanical de-icing cannot yet be completely achieved with the test parameters described.

From the test results, it can be deduced that the coordination between the mechanical and thermal effects must be improved. First of all, a reliable actuation of the SMA wire must be ensured by using higher currents, so that higher wire temperatures are achieved. This requires a more powerful current source. Alternatively, SMAs with lower transition temperatures can be used to reliably activate these at lower wire temperatures. The third possible arrangement is to place the wire further away from the surface. This reduces heat dissipation to the surface and allows the wire to reach higher stationary temperatures.

The aim of the design was to achieve the highest possible heat conduction but it turns out to be insufficiently differentiated against the background of the test results. The test shows that the heat flow to the surface is sufficient to melt the ice at an ambient temperature of about −15 °C. However, de-icing of the entire surface cannot be observed. Further investigations will therefore also consider the temporal behavior of the temperatures in the wire and on the surface.

7. Discussion

The starting point of the study is the hypothesis that the temperature rise and the resulting deformation of an SMA can be used to build up a de-icing system. Due to its coupled thermal and mechanical properties, SMA naturally provides a hybrid system. The basic idea is to divide the surface to be de-iced into individual de-icing segments. In this study, simulations and tests are first carried out on a single de-icing segment.

The initial examinations of the finished sample are conducted at room temperature. Here the temperature change and the deformation of the surface in relation to the activation of SMA are investigated. The elastomer deformation is determined at six points on the surface. Remarkably, the measured data confirm that the numerical results on the mechanical behavior provided a highly reliable approximation.

Further experiments are performed at −15 °C in a freezer. First, the system is tested without an ice layer. After three minutes of activation, the embedded thermocouple reaches 60 °C, while the highest surface temperature is 70 °C. The most striking result to emerge from the data is that the temperature measurement does not work reliably. The reason is that the resistances of the crimp connections are not the same due to the electrical contact resistances. This of course has a disadvantage because detecting the wire temperature plays a key role in the subsequent control of the wire actuation cycle.

In order to understand the de-icing capability of the sample, it is tested at −15 °C with an ice layer but without aerodynamical loading. Although SMA has adequate properties for the task, it has been observed that thermo-mechanical de-icing has not been fully accomplished. This is mainly due to the fact that the coordination of the thermal and mechanical effects does not yet occur as expected. The main reason is that the position of the wire is too close to the surface.

Contrary to expectations, no sufficient surface deformation is achieved. In the middle of the elastomer membrane, there is a disc-shaped ice layer without breakage. No significant temperature increase is found at the corners of the membrane surface, as the thermal imaging camera shows. In addition, the ice layer outside the ring remains intact. Another limitation of this study is that the sample is examined individually. With multiple segments, as is actually planned, the size of the non-deiced zones should also be considered.

8. Conclusion

In this study, an SMA based de-icing system is investigated from a hypothesis to a functional sample. The effects of the geometric and material parameters on the behavior of the functional sample are revealed using the parameter study. The functional interrelationships have been thoroughly investigated experimentally and led to important findings.

The system is evaluated under extreme cases to perceive the reaction of the sample against ice layers with different thicknesses. In the first case, a rigid ice layer, which corresponds approximately to a very thick ice layer, is considered. The second case is without any ice layer on the surface.

The initial test of a functional sample is performed at room temperature. The mechanical deformation is observed with a steady amperage of 2.6 A ($U = 2.1$ V).

The tests at −15 °C performed with and without an ice layer show that the heat conduction is high, and therefore the ice layer is partially melted, although the thermal effect has only been intended to weaken the ice adhesion.

In conclusion, the findings of this study support the idea, that SMA is applicable for a de-icing system, however, both the mechanical as well as thermal effects must be precisely coordinated. Further research is needed to ensure that both effects have an equal impact. In addition, the higher current at low temperatures should be used so that SMA can reach A_f without difficulty. It would also be possible to investigate an SMA with a lower transition temperature as long as it is not already reached in normal operation due to warm environmental conditions.

For reliable temperature control, a control system based on the change in resistance should be preferred. This avoids an integrated thermocouple, which is difficult to set on the same position every time.

The influence of the two-stage casting process on the elastomer's strength and fatigue properties at the contact surface is still to be determined. If there is an influence, alternatives to two-stage casting or ways to minimize the fatigue effect must be found. In addition, setting the pretension of the wire in the functional sample is currently still a source of inaccuracy and lack of repeatability.

This study is the first step towards enhancing the understanding of the simulation model, the manufacturing process and the experimental methodology. It will allow further optimization of the thermo-mechanical de-icing effect in future development steps.

ORCID iDs

Ozan Tamer https://orcid.org/0000-0001-6030-3298
Alexander Kyriazis https://orcid.org/0000-0003-0251-2643

References

[1] Gerardi J, Ingram R and Catarella R 2013 A shape memory alloy based de-icing system for aircraft. *33rd Aerospace Sciences Meeting and Exhibit* p 454
[2] Adams L J 1996 Deicer assembly utilizing shaped memory metals *US Patent* 5,558,304
[3] Ingram R B and Gerardi J J 1997 Shape memory alloy de-icing technology *US Patent* 5,686,003
[4] Myose R Y, Horn W J, Hwang Y, Herrero J, Huynh C and Boudraa T 1999 Application of shape memory alloys for leading edge deicing *SAE Technical Paper* (https://doi.org/10.4271/1999-01-1585)
[5] Pinto F, Ciampa F, Meo M and Polimeno U 2012 Multifunctional SMArt composite material for *in situ* NDT/SHM and de-icing *Smart Materials and Structures* **21** 105010
[6] Sullivan D B, Righi F, Hartl D J and Rogers J 2013 Shape memory alloy rotor blade deicing *54th AIAA/ASME/ASCE/AHS/ASC Structures, Structural Dynamics, and Materials Conf.* (https://doi.org/10.2514/6.2013-1915)
[7] Liu X, Xing Y and Zhao L 2018 Study of shape memory alloy de-icing device for nonrotating components of aircrafts *IOP Conference Series: Materials Science and Engineering*. **394** 032106
[8] Mingione G, Barocco M, Denti E, Bindi F G and French D 1997 *Flight in icing conditions* Direction generale de l'aviation civile, DGAC Tech. Rep.
[9] Scholz D 2017 Eis-und Regenschutz., Hochschule Hamburg: Lecture notes on Aircraft systems, Chapter 9.
[10] Pahl G and Beitz W 2013 *Engineering Design: A Systematic Approach* (London: Springer) (https://doi.org/10.1007/978-1-84628-319-2)
[11] Lagoudas D 2008 *Shape Memory Alloys. Modeling and Engineering Applications* (New York: Springer) (https://doi.org/10.1007/978-0-387-47685-8)
[12] Langbein S and Czechowicz A 2013 Konstruktionspraxis Formgedächtnistechnik *Potentiale—Auslegung—Beispiele* (Wiesbaden: Springer) (https://doi.org/10.1007/978-3-8348-2343-4)
[13] Palacios J L 2008 Design, fabrication and testing of an ultrasonic de-icing system for helicopter rotor blades *PhD Thesis* Pennsylvania State University
[14] Riahi M M, Marceau D, Laforte C and Perron J 2011 The experimental/numerical study to predict mechanical behaviour at the ice/aluminium interface *Cold Reg. Sci. Technol.* **65** 191–202
[15] Schulz M 2016 *Zeitabhängigkeit der Eisadhäsionsfestigkeit* (Braunschweig: Deutsches Zentrum für Luft-und Raumfahrt) Doctoral dissertation
[16] DeGarmo E P, Black J T, Kohser R A and Klamecki B E 2008 *Materials and Process in Manufacturing* 10th edn (Hoboken, NJ : Wiley) 13-978-0470-05512-0
[17] Rösler J, Bäker M and Harders H 2007 *Mechanical Behaviour of Engineering Materials* (Berlin Heidelberg: Springer) (https://doi.org/10.1007/978-3-540-73448-2)
[18] Bonnet M 2009 *Kunststoffe in der Ingenieuranwendung-Verstehen und Zuverlässig Auswählen* 1st edn (Wiesbaden: Vieweg+Teubner) (https://doi.org/10.1007/978-3-8348-9303-1)
[19] Weiss R and Osen E 2001 FEM-berechnung von elastomerbauteilen–werkstoffspezifische grundlagen *Automobiltechnische Zeitschrift* **103** S.242–6
[20] Dynalloy, Inc. 2007 Technical Characteristics of Flexinol Actuator Wires.